Non-classical nuclei and growth kinetics of Cr precipitates in FeCr alloys during ageing

2014 Modelling Simul. Mater. Sci. Eng. 22 025002

(http://iopscience.iop.org/0965-0393/22/2/025002)

IOP Publishing Modelling and Simulation in Materials Science and Engineering

Modelling Simul. Mater. Sci. Eng. **22** (2014) 025002 (13pp) doi:10.1088/0965-0393/22/2/025002

Non-classical nuclei and growth kinetics of Cr precipitates in FeCr alloys during ageing

Yulan Li[1], Shenyang Hu[1], Lei Zhang[2] and Xin Sun[1]

[1] Pacific Northwest National Laboratory, 902 Battelle Boulevard, Richland, WA 99352, USA
[2] Beijing International Center for Mathematical Research, Peking University, Beijing 100871, People's Republic of China

E-mail: yulan.li@pnnl.gov

Received 13 August 2013, revised 11 November 2013
Accepted for publication 25 November 2013
Published 10 January 2014

Abstract

In this manuscript, we have quantitatively calculated the thermodynamic properties of the critical nuclei of Cr precipitates in FeCr alloys. The concentration profiles of the critical nuclei and nucleation energy barriers were predicted by the constrained shrinking dimer dynamics method. It is found that Cr concentration distribution in the critical nuclei strongly depends on the overall Cr concentration as well as on the temperature. The critical nuclei are non-classical because the concentration in the nuclei is smaller than the thermodynamic equilibrium value. These results are in agreement with atomic probe observation. The growth kinetics of both classical and non-classical nuclei was investigated by the phase-field approach. The simulations of critical nucleus evolution showed a number of interesting phenomena: (1) a critical classical nucleus first shrinks toward its non-classical nucleus and then grows; (2) a non-classical nucleus has much slower growth kinetics at its earlier growth stage compared to the diffusion-controlled growth kinetics and (3) a critical classical nucleus grows faster at the earlier growth stage than does a non-classical nucleus. All of these results demonstrate that it is critical to introduce the correct critical nuclei in order to correctly capture the kinetics of precipitation.

Keywords: critical nucleus, nucleation barrier, dimer method, phase-field approach, FeCr alloys

(Some figures may appear in colour only in the online journal)

1. Introduction

High chromium ferritic/martensitic steels are preferred candidates for structural materials in fusion and advanced fission reactor components [1]. The addition of Cr has a positive effect on mechanical, corrosion and radiation resistance properties. However, it is well known that FeCr alloys undergo thermal- and irradiation-induced phase separation from the solid solution into a Fe-rich phase and a Cr-rich phase in the temperature range of 300–550 °C [2, 3]. The phase separation causes material property degradation, such as embrittlement and stress corrosion cracking [2, 4]. A fundamental understanding of the thermodynamics, mechanism and kinetics of phase separation is of technological importance in predicting microstructure evolution and material property degradation.

Phase separation in FeCr solid solutions takes place through two different mechanisms, which are: (1) spinodal decomposition and (2) Cr-rich phase nucleation and growth. Which mechanism operates depends on Cr concentration and ageing temperature. Spinodal decomposition can be naturally simulated using atomistic and field theoretical methods by introducing any fluctuation of temperature, composition and/or order parameters. However, modeling nucleation is generally believed to be one of the most challenging issues. For example, the phase-field approach is a very powerful simulation tool to predict the microstructure evolution during phase separation [5]. Although the phase-field approach takes into account the energy changes during nucleation (such as a bulk free energy decrease that is proportional to the nucleus volume, an interfacial energy increase which is proportional to interfacial area, and long-range interaction energies (e.g. elastic energy)), it is unable to simulate the nucleation process because the phase-field approach assumes that the microstructure evolution is driven by the energy minimization while the nucleation needs to overcome an energy barrier. Therefore, in order to simulate the phase separation, phase-field simulations have to introduce critical nuclei into the simulation cells. According to classical nucleation theory, the thermodynamic and kinetic information including the critical nucleus radius, nucleation barrier, and nucleation rate can be calculated once we know the chemical free energy, interfacial energy and long-range interaction energy. However, experiments [6] and kMC simulations [7] have all shown that the nucleation of Cr precipitates in FeCr alloys is a non-classical nucleation; that is, the Cr concentration inside the nucleus is not the same as the thermal equilibrium concentration, particularly when the FeCr alloys have high supersaturations. The thermodynamic and kinetic information of non-classical nuclei in FeCr alloys are lacking for the phase-field simulations. Furthermore, it is unknown how the critical nucleus from non-classical nucleation and classical nucleation affects growth kinetics.

In this work, we will quantitatively calculate the thermodynamic properties of critical nuclei with the chemical free energy and interfacial energy assessed from thermodynamic calculation and atomistic simulations [8, 9]. The constrained shrinking dimer dynamics (CSDD) method is employed to search for the critical concentration profiles of the nuclei in FeCr alloys in terms of temperature and overall Cr concentration. The growth kinetics of Cr precipitates with classical and non-classical nucleus profiles is examined by the phase-field approach.

2. Phase-field model of Cr precipitation in FeCr alloys

In FeCr alloys, Cr precipitates are Cr-rich phases that have the same structure as the matrix phase (i.e. bcc FeCr solid solution). Therefore, the precipitate microstructure in bcc FeCr alloys can be uniquely described by Cr concentration. In the framework of the phase-field approach, the concentration of Cr, $C_{\mathrm{Cr}}(\boldsymbol{r}, t)$, is employed as the phase-field variable where

$\boldsymbol{r} = (r_1, r_2, r_3)$ is the spatial coordinate and t is time. Compared with the Cr solubility in FeCr alloys, thermal equilibrium vacancy concentration is very small and is, therefore, ignored in the present model. Consequently, the concentration of Fe is $1 - C_{\mathrm{Cr}}$. Due to the low lattice mismatch, the elastic energy contribution in the FeCr system is negligible and omitted in this study. Therefore, the total free energy of the binary system can be expressed as

$$E(C_{\mathrm{Cr}}, T) = \int_V \left[\frac{NA_0}{\Omega_0} f(C_{\mathrm{Cr}}, T) + \frac{\kappa}{2} |\nabla C_{\mathrm{Cr}}|^2 \right] \mathrm{d}V, \tag{1}$$

where $\nabla = (\partial/\partial r_1 + \partial/\partial r_2 + \partial/\partial r_3)$ is the gradient operator and V is the volume of the considered system. $N = 6.022 \times 10^{23}$ (atom mol^{-1}), is the Avogado's constant. $\Omega_0 = 1.4087 \times 10^{-5}$ [m^3 mol^{-1}] is the molar volume of bcc Fe, constant $A_0 = 1.602 \times 10^{-19}$ (J eV^{-1}). $f(C_{\mathrm{Cr}}, T)$ is the chemical free energy density per atom in electron volts (eV) and κ is the interfacial energy coefficient.

Since the concentration C_{Cr} is a conserved field variable, its temporal evolution is described by the Cahn–Hillard equation:

$$\frac{\partial C_{\mathrm{Cr}}}{\partial t} = -\nabla \cdot \left(-M \nabla \frac{\delta E}{\delta C_{\mathrm{Cr}}} \right) = \nabla \cdot M \nabla \left[\frac{NA_0}{\Omega_0} \frac{\partial f}{\partial C_{\mathrm{Cr}}} - \kappa \nabla^2 C_{\mathrm{Cr}} \right], \tag{2}$$

where M is the mobility of C_{Cr} and related to Cr atom diffusivity, D, as $M = D\Omega_0/(\Re T)$ with $\Re$ being the gas constant of $\Re = 8.314$J/ (mol K). To numerically solve equation (2), the following normalizations are used: $t^* = t/t_0$, $t_0 = l_0^2 \Omega_0 / NA_0 M$, $r_i^* = r_i/l_0$, $\kappa^* = \kappa\Omega_0/NA_0 l_0^2$, $\nabla = (\partial/\partial r_1, \partial/\partial r_2, \partial/\partial r_3) = (1/l_0)\left(\partial/\partial r_1^*, \partial/\partial r_2^*, \partial/\partial r_3^*\right) = (1/l_0)\nabla^*$. l_0 is a characteristic length. Therefore, equation (2) is rewritten as

$$\frac{\partial C_{\mathrm{Cr}}}{\partial t^*} = \nabla^{*2} \left[\frac{\partial f}{\partial C_{\mathrm{Cr}}} - \kappa^* \nabla^{*2} C_{\mathrm{Cr}} \right]. \tag{3}$$

Equation (3) will be numerically solved by the semi-implicit Fourier-spectral method [10] under periodic boundary conditions.

3. Assessment of thermodynamic properties

3.1. Chemical free energy

To predict Cr precipitate formation and growth, or to solve the evolution equation (3), the free energy density $f(C_{\mathrm{Cr}}, T)$ is needed. Thanks to the efforts of many people, an analytical free energy density has now become available for the FeCr system [8, 9]:

$$f(C_{\mathrm{Cr}}, T) = G(1 - C_{\mathrm{Cr}}, T), \tag{4}$$

$$G(x, T) = G_0(x, T)\frac{T}{T_0} + H_a(x) - H_b(x)T\log T - H_c(x)T^2 + H_d(x)\frac{T^3}{2} + H_e(x)T + k_{\mathrm{B}}T\left[x\log x + (1-x)\log(1-x)\right], \tag{5}$$

$$H_a(x) = x(1-x)\sum_{i=0}^{5} a_i (1-2x)^i + a_6 x + a_7 (1-x), \tag{6}$$

$$H_{\xi\in\{b,c,d\}}(x) = \sum_{i=0}^{3} \xi_i (1-x)^i, \tag{7}$$

$$H_e(x) = -\frac{H_a(x)}{T_0} + H_b(x)\log T_0 + H_c(x)T_0 + H_d(x)\frac{T_0^2}{2}, \tag{8}$$

$$G_0(x) = x(1-x)\sum_{i=0}^{5} f_i (1-2x)^i + f_6 x + f_7 (1-x), \tag{9}$$

Table 1. Coefficients for the FeCr free energy given in equations (4)–(9) [9].

ξ	a	b	c	d	f
ξ_0	0.3856	2.630×10^{-4}	3.145×10^{-9}	-1.7601×10^{-13}	0.3817
ξ_1	0.0973	4.696×10^{-5}	-2.203×10^{-8}	5.579×10^{-12}	0.1007
ξ_2	−0.0467	-4.959×10^{-5}	3.960×10^{-8}	-5.935×10^{-12}	−0.0485
ξ_3	0.1945	1.133×10^{-5}	-3.090×10^{-8}	1.229×10^{-11}	0.1541
ξ_4	−0.1856				−0.1684
ξ_5	0.0044				0.0416
ξ_6	−4.1231				−4.1671
ξ_7	−3.8366				−3.8602

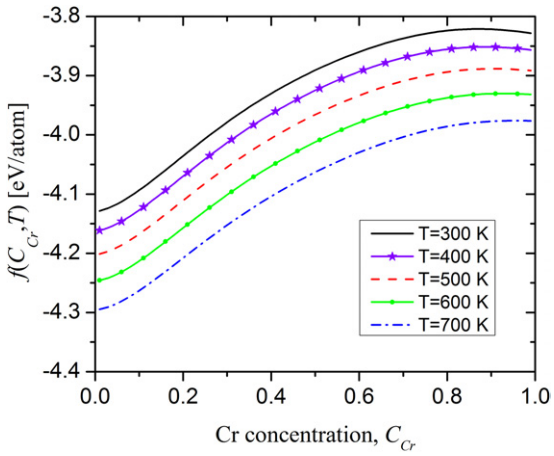

Figure 1. Chemical free energy of FeCr alloys.

where $T_0 = 410\,\mathrm{K}$, $k_\mathrm{B} = 8.6173 \times 10^{-5}\,\mathrm{eV\,K^{-1}}$ is the Boltzmann constant, and $x = 1 - C_\mathrm{Cr}$ is the concentration of Fe. The corresponding coefficients are listed in table 1. At the given temperatures, the free energies are plotted in figure 1.

With the free energy density $f(C_\mathrm{Cr}, T)$, we calculate the Cr solubility, spinodal concentrations, and equilibrium concentration of Cr precipitate in the FeCr alloys at different temperatures. The chemical free energy $f(C_\mathrm{Cr}, T)$ has a common tangent at the Cr solubility in FeCr solid solution and Cr equilibrium concentration in Cr precipitate. The spinodal concentration is associated with the inflection point of $f(C_\mathrm{Cr}, T)$. Table 2 lists the Cr solubility and spinodal concentrations in Fe-rich side and Cr thermodynamic equilibrium concentration in Cr precipitates.

3.2. Interfacial energy

In the phase-field model described in equations (1) and (2), both the chemical free energy $f(C_\mathrm{Cr}, T)$ and the gradient energy contribute the interfacial energy. For given characteristic length l_0 and gradient coefficient κ, the interfacial energy of a flat interface can be numerically calculated. To do so, we put a precipitate at the center of a one dimensional (1D) simulation cell ($512l_0 \times l_0 \times l_0$) and let the system approach equilibrium through Cr diffusion. At the equilibrium state, the equilibrium concentrations in both precipitate and matrix, as well as the

Table 2. Cr solubility and spinodal concentrations in Fe-rich side and Cr equilibrium concentration in Cr precipitates.

Temperature (K)	Cr solubility ($C_{\mathrm{Cr}}^{\mathrm{M,\,eq}}$)	Cr spinodal concentration	Cr equilibrium concentration in Cr precipitate ($C_{\mathrm{Cr}}^{\mathrm{P,\,eq}}$)
300	0.041 99	0.190 49	1.0
400	0.048 29	0.194 22	1.0
500	0.055 01	0.198 40	0.999 98
600	0.062 23	0.203 09	0.999 89
700	0.070 08	0.208 40	0.999 58

Table 3. Interfacial energies at different temperatures.

Temperature (K)	This work with $\kappa^* = 0.8\,\mathrm{eV/atom}$ $l_0 = 0.287\,\mathrm{nm}$ ($\mathrm{J\,m^{-2}}$)	Work [9, 11] ($\mathrm{J\,m^{-2}}$)
300	0.5334	0.4049
400	0.5016	0.3910
500	0.4811	0.3762
600	0.4382	0.3606
700	0.4093	0.3441

equilibrium interface concentration profile, are reached. The interfacial energy can then be numerically calculated with the equilibrium concentration profile by

$$\gamma = \frac{1}{2}\frac{NA_0}{\Omega_0}\int_V \left[\left\{f(C_{\mathrm{Cr}},T) - \left[f(C_{\mathrm{Cr}}^{\mathrm{M,eq}},T) + f'(C_{\mathrm{Cr}}^{\mathrm{M,eq}},T)(C_{\mathrm{Cr}} - C_{\mathrm{Cr}}^{\mathrm{M,eq}})\right]\right\} + \frac{1}{2}\kappa^*\left|\nabla^* C_{\mathrm{Cr}}\right|^2\right]\mathrm{d}V, \tag{10}$$

where the $1/2$ factor outside the integral is due to the fact that there are two interfaces in the one-dimensional model. $f(C_{\mathrm{Cr}}^{\mathrm{M,eq}},T)$ and $f'(C_{\mathrm{Cr}}^{\mathrm{M,eq}},T)$ are the corresponding function and its derivative with respect to C_{Cr} at $C_{\mathrm{Cr}} = C_{\mathrm{Cr}}^{\mathrm{M,eq}}$. Through tailoring the characteristic length l_0 and gradient coefficient κ^*, the phase-field model can correctly describe the interfacial energy of Cr precipitates. In the general case, the interfacial energy is anisotropic. Then, the gradient coefficient κ is a tensor. The same method can be used to determine the tensor κ.

By taking l_0 as the α-Fe lattice parameter (i.e. $l_0 = 0.287\,\mathrm{nm}$ and $\kappa^* = 0.8\,\mathrm{eV/atom}$), the corresponding interface energies are calculated with equation (10) for different temperatures. The results are listed in table 3 and compared with those obtained by Schwen *et al* [9] through fitting the results from Sadigh and Erhart [11]. It is seen that the interfacial energy from this work is slightly larger than that from the previous studies. This can be adjusted by taking a smaller l_0. The corresponding equilibrium profiles for an average concentration of $C_{\mathrm{Cr}} = 15.8\%$ at different temperatures are given in figure 2. From the inset of the figure, we can see that the phase-field model can well predict the equilibrium concentrations.

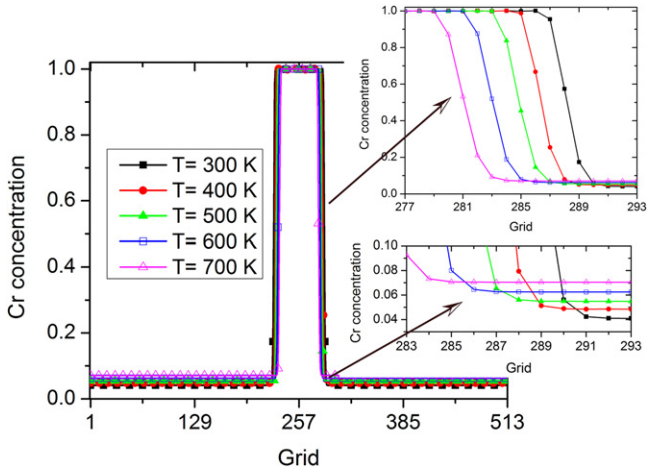

Figure 2. Equilibrium profiles of Cr precipitates of 1D simulation model when Cr average concentration is $c_0 = 0.158$. The two insets display the Cr concentration at the interface and the matrix phase.

4. CSDD

In recent years, high-performance numerical methods have been proposed to find critical nucleus [12] and applied to the nucleation in solid-state phase transformation [13]. In particular, the shrinking dimer dynamics (SDD) [14] and its extension on a constrained manifold, CSDD [15], have been successfully used to efficiently compute the saddle point associated with an energy functional. Here we apply the CSDD to predict the critical nuclei of Cr precipitates in FeCr alloys basing on the free energy and interfacial energy given in the previous section. The constraint of the current model comes from the mass conservation; that is,

$$G\left(C_{\mathrm{Cr}}\right) = \int_V \left[C_{\mathrm{Cr}}\left(\boldsymbol{r}, T\right) - c_0\right] \mathrm{d}V = 0. \tag{11}$$

To construct the dimer system, we let $C_{\mathrm{Cr}(1)}$ and $C_{\mathrm{Cr}(2)}$ be the two end points of a dimer with a length of $l = |C_{\mathrm{Cr}(1)} - C_{\mathrm{Cr}(2)}|$. The dimer orientation is given by a unit vector v, so that $C_{\mathrm{Cr}(1)} - C_{\mathrm{Cr}(2)} = lv$. The rotation center of a dimer is defined as $C^{\alpha}_{\mathrm{Cr}} = (1-\alpha)C_{\mathrm{Cr}(1)} + \alpha C_{\mathrm{Cr}(2)}$, where the parameter $\alpha \in [0, 1]$. So the geometric center (midpoint of the dimer) corresponds to $\alpha = 0.5$. Thereby, $C_{\mathrm{Cr}(1)} = C^{\alpha}_{\mathrm{Cr}} + \alpha l v$, $C_{\mathrm{Cr}(2)} = C^{\alpha}_{\mathrm{Cr}} - (1-\alpha) l v$.

To enforce the constraint, CSDD uses the projected natural force, which is the negative gradient force projected on the tangential hyper plane of the constraint; that is,

$$\tilde{F}\left(C_{\mathrm{Cr}}\right) = \frac{\delta E^*\left(C_{\mathrm{Cr}}\right)}{\delta C_{\mathrm{Cr}}} - \frac{1}{V}\int_V \frac{\delta E^*\left(C_{\mathrm{Cr}}\right)}{\delta C_{\mathrm{Cr}}} \mathrm{d}V = \left(\frac{\partial f}{\partial C_{\mathrm{Cr}}} - \kappa^* \nabla^{*2} C_{\mathrm{Cr}}\right) - \frac{1}{V}\int_V \left(\frac{\partial f}{\partial C_{\mathrm{Cr}}} - \kappa^* \nabla^{*2} C_{\mathrm{Cr}}\right) \mathrm{d}V, \tag{12}$$

with $E^*(C_{\mathrm{Cr}}) = (\Omega_0/NA_0)E(C_{\mathrm{Cr}}) = \int_V \left[f(C_{\mathrm{Cr}}, T) + (\kappa^*/2)\,|\nabla^* C_{\mathrm{Cr}}|^2\right] \mathrm{d}V$. Following the SDD, the formulation of the CSDD is given by [15]

$$\begin{aligned} \mu_1 \frac{\partial C_{\mathrm{Cr}}^{\alpha}}{\partial t} &= \left(I - 2vv^{\mathrm{T}}\right)\left[(1-\alpha)\,\tilde{F}_1 + \alpha \tilde{F}_2\right], \\ \mu_2 \frac{\partial v}{\partial t} &= \left(I - vv^{\mathrm{T}}\right)\frac{\left(\tilde{F}_1 - \tilde{F}_2\right)}{l}, \\ \mu_3 \frac{\mathrm{d}l}{\mathrm{d}t} &= -\frac{\mathrm{d}E_{\mathrm{dimer}}(l)}{\mathrm{d}l}, \end{aligned} \tag{13}$$

with the relaxation constants μ_1, μ_2, μ_3. $\tilde{F}_1 = \tilde{F}\left(C_{\mathrm{Cr}(1)}\right)$ and $\tilde{F}_2 = \tilde{F}\left(C_{\mathrm{Cr}(2)}\right)$. The first equation of the CSDD in (13) represents the translation step of the dimer, and the operator $(I - 2vv^{\mathrm{T}})$ is the Householder mirror reflection, which reverses the component of the negative gradient force at v direction. The second equation in (13) is the rotation step of the CSDD. The third equation in (13) follows the gradient flow of the dimer energy, resulting in the dimer shrinking over time and the solution of (13) converging to an exact saddle point. In this work, we have decided to use an auxiliary function $E_{\mathrm{dimer}}(l) = l^2/2$, which gives an exponential decay of the dimer length.

The initial condition of the CSDD needs to satisfy the following compatibility assumption: $G\left(C_{\mathrm{Cr}}^0\right) = 0$, $|v_0(\boldsymbol{r})| = 1$, $\int_V v_0(\boldsymbol{r})\,\mathrm{d}V = 0$. The $|v_0|$ represents the magnitude of vector v_0. One straightforward way to implement the time discretization of the CSDD is to apply the modified forward Euler scheme:

$$\begin{cases} C_{\mathrm{Cr}}^{\alpha,n+1} = C_{\mathrm{Cr}}^{\alpha,n} + \frac{\Delta t}{\mu_1}\left(I - 2v^n\,(v^n)^{\mathrm{T}}\right)\left[(1-\alpha)\,\tilde{F}\left(C_{\mathrm{Cr}(1)}^n\right) + \alpha \tilde{F}\left(C_{\mathrm{Cr}(2)}^n\right)\right], \\ \bar{v}^{n+1} = v^n + \frac{\Delta t\left[\tilde{F}\left(C_{\mathrm{Cr}(1)}^n\right) - \tilde{F}\left(C_{\mathrm{Cr}(2)}^n\right)\right]}{\mu_2 l^n}, \qquad v^{n+1} = \frac{\bar{v}^{n+1}}{\left\|\bar{v}^{n+1}\right\|}, \\ l^{n+1} = \dfrac{l^n}{1 + \Delta t/\mu_3}, \end{cases} \tag{14}$$

which performs a normalization on v at each iteration for the dimer rotation step so that the scheme improves the local stability and optimal error reduction rate. To further improve the stability of Euler method, and to allow the larger time step in the algorithm, we employ a semi-implicit splitting scheme for the CSDD, in which the principal linear operator is treated implicitly to reduce the associated stability constraint while the nonlinear terms are still treated explicitly to avoid the expensive process of solving nonlinear equations at each time step. The Fourier-spectral method is used for the spatial discretization to achieve exponential convergence in space. In our calculations, $\mu_1 = \mu_2 = \mu_3 = 1, \alpha = 0.5$.

5. Non-classical critical nuclei and nucleation barriers of Cr precipitates in FeCr alloys

Here, we assume that the interfacial energy is isotropic and, therefore, the critical nucleus will be a sphere in a real three dimensional (3D) space. Experiments [6] have also shown that the Cr precipitates in FeCr alloys have a spherical shape. Since the chemical free energy of equation (4) depends on Cr concentration and temperature, the critical nucleus profile will also vary with Cr overall concentration and temperature. To calculate the concentration profile of critical nuclei, we consider a 3D simulation cell of $64l_0 \times 64l_0 \times 64l_0$. For a given temperature (T) and Cr overall concentration (c_0), the critical nucleus profile is obtained by solving the CSDD equations. Figure 3 plots the critical profile dependence on the Cr overall concentration (c_0) and temperature (T). We can see that the concentrations inside the nuclei

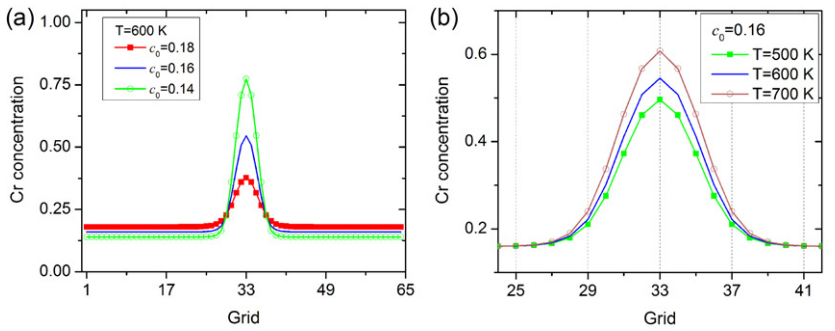

Figure 3. Cr nucleus profiles at: (*a*) different Cr overall concentration (c_0); and (*b*) different temperature (T). The plots illustrate the Cr concentration distribution along the diameter of the spherical nuclei. In (*b*), the plots are zoomed in the nucleus center areas in order to give a better resolution.

are much smaller than the equilibrium concentration of Cr precipitates (i.e. $C_{\mathrm{Cr}}^{\mathrm{P,\,eq}} \approx 1$) that are calculated from the equilibrium phase diagram. Experiments of atom probe observation [6] have also demonstrated that the Cr concentration in the nuclei does not have to be its bulk equilibrium value; therefore, the critical nucleus of Cr precipitate is non-classical. Although it is hard to define the critical size of a nucleus, we can clearly see that Cr content inside the nuclei increases with the decrease of the Cr overall concentration and the increase of temperature.

To validate that the concentration profiles predicted from the CSDD are critical profiles, we numerically examine the evolution of the nucleus. Figure 4(*a*) displays the profiles of the critical nuclei for $c_0 = 0.16$ at $T = 500$ K and $T = 501$ K, respectively. Although the nucleus at $T = 501$ K is very slightly larger than the one at $T = 500$ K, the difference between them is hardly identified from the figure. By introducing the nuclei into the phase-field simulation cells and evolving the phase-field equation (3) at the corresponding temperatures, we find from figures 4(*b*) and (*c*) that both nuclei are stable and grow. If the slightly small nucleus obtained at $T = 500$ K is used for $T = 501$ K, the nucleus becomes unstable and shrinks (as shown in figure 4(*d*)). These results numerically prove that the CSDD method can provide the critical nucleus concentration profiles. Of course, the validation of the critical profile (that is, the saddle point of the energy functional (1)) can be performed by introducing a small perturbation p_0 as $C_{\mathrm{Cr}}(\boldsymbol{r}) = C_{\mathrm{Cr}}^{\mathrm{saddle}}(\boldsymbol{r}) + p_0 v^{\mathrm{saddle}}(\boldsymbol{r})$, where $C_{\mathrm{Cr}}^{\mathrm{saddle}}(\boldsymbol{r})$ and $v^{\mathrm{saddle}}(\boldsymbol{r})$ are the solution of equation (14). A small value p_0 can drive the profile of $C_{\mathrm{Cr}}(\boldsymbol{r})$ away from its saddle point $C_{\mathrm{Cr}}^{\mathrm{saddle}}(\boldsymbol{r})$ by either growing or shrinking through substituting $C_{\mathrm{Cr}}(\boldsymbol{r})$ into equation (3) and evolving it for a long enough time. In practice, the numerical error included in $C_{\mathrm{Cr}}^{\mathrm{saddle}}(\boldsymbol{r})$ through numerical searching is already large enough to make the nucleus grow or shrink.

It is known that the critical nucleus is associated with the concentration fluctuation that has the minimum free energy increase amongst all of the fluctuations that lead to growth. In the following, we calculate the energy excess, the energy difference between the system with a critical nucleus and the original supersaturated system with uniform concentration,

$$E_{\mathrm{excess}} = F \Big/ \left(\frac{l_0^3 N A_0}{\Omega_0} \right) = \int_{V^*} \left[f(C_{\mathrm{Cr}}, T) + \frac{1}{2}\kappa^* \left| \nabla^* C_{\mathrm{Cr}} \right|^2 - f(c_0, T) \right] \mathrm{d}V^*. \tag{15}$$

Actually, E_{excess} is the nucleation energy barrier. The results of E_{excess} for different temperatures and concentrations are given in figure 5. It is clearly seen that the nucleation barrier decreases with decreasing temperature and increasing average Cr concentration. The nucleation barrier approaches to zero when Cr concentration approaches the spinodal concentration $c_0 = 0.20$.

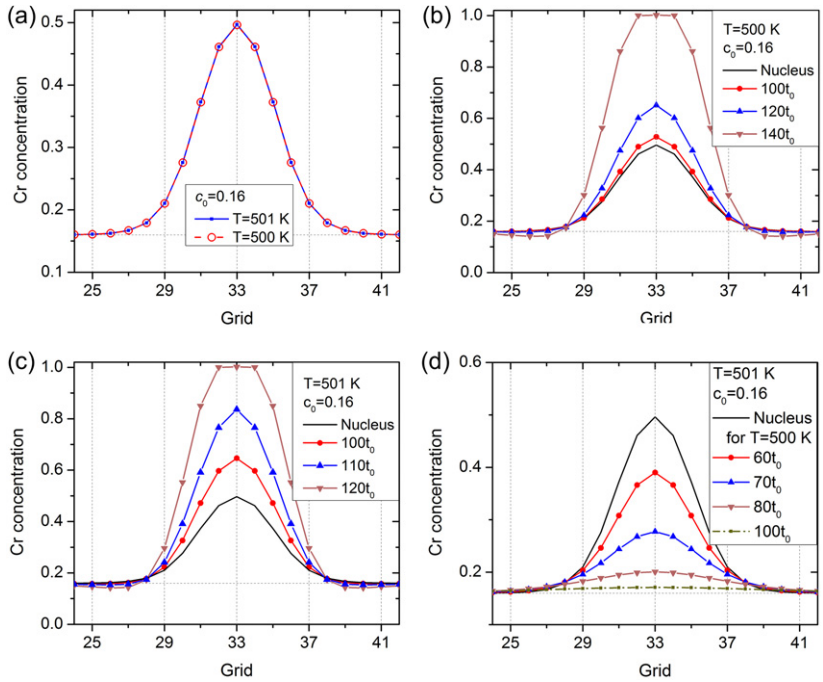

Figure 4. Critical nucleus concentration profiles for $c_0 = 0.16$ at $T = 500\,\mathrm{K}$ and 501 K and their temporal evolution: (*a*) critical profiles; (*b*) evolution of the nucleus of $T = 500\,\mathrm{K}$ at $T = 500\,\mathrm{K}$; (*c*) evolution of the nucleus of $T = 501\,\mathrm{K}$ at $T = 501\,\mathrm{K}$; and, (*d*) evolution of $T = 500\,\mathrm{K}$ nucleus at $T = 501\,\mathrm{K}$.

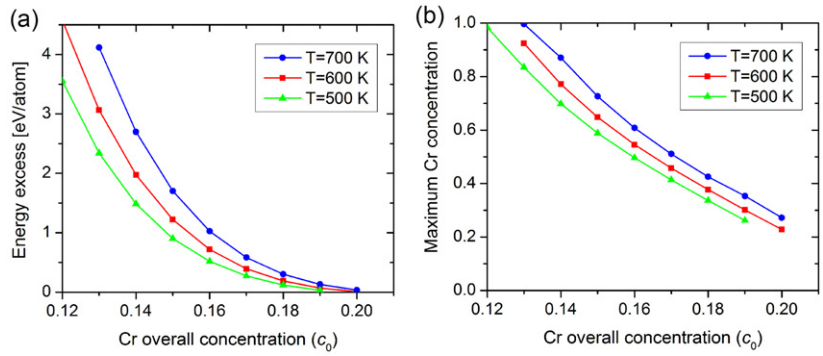

Figure 5. (*a*) The energy excess (nucleation barrier) required for the formation of a critical nucleus; and (*b*) the maximum concentrations inside the critical nuclei at different temperature and different overall Cr concentration.

This is in agreement with the spinodal decomposition theory. The maximum Cr concentrations of the nuclei corresponding to figure 5(*a*) are plotted in figure 5(*b*). Both the nucleation barrier and the maximum value of a critical nucleus strongly depend on the temperature and Cr concentration. These thermodynamic properties are important to calculate the nucleation rates and introduce the correct critical nuclei in the phase-field modeling of precipitation kinetics.

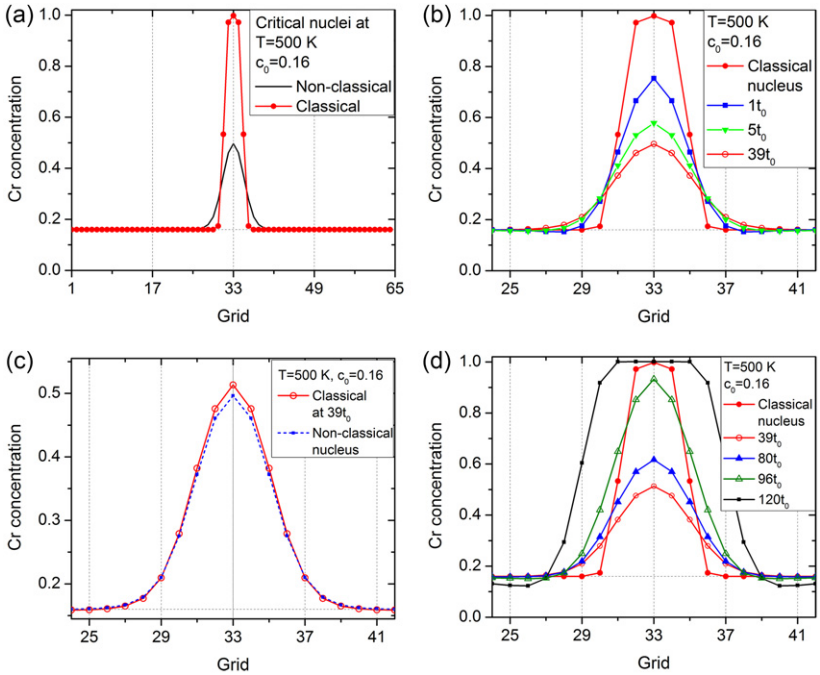

Figure 6. Classical nucleus profile of $T = 500$ K and $c_0 = 0.16$ and its evolution growth with time: (a) comparison of critical nucleus profiles between the classical nucleus and non-classical nucleus; (b) nucleus evolution at its shrinking stage; (c) comparison of the non-classical nucleus and the classical nucleus at the stage with lowest concentration at its center and (d) nucleus evolution at its growth stage.

6. Growth kinetics of classical and non-classical nuclei

In classical nucleation theory, the concentration inside the critical nucleus is assumed to be $C_{\mathrm{Cr}}^{\mathrm{P,eq}}$, which is the equilibrium concentration of the precipitate phase. However, as shown in the previous section, the concentration in non-classical critical nucleus is much less than the equilibrium concentration. So, the question is, how do the critical concentration profiles affect their growth kinetics? To answer this question, the growth kinetics of the critical nuclei with classical and non-classical concentration profiles is simulated with the phase-field model. In the simulations, we first numerically determine the critical concentration profile of a classical nucleus by examining the growth and shrinkage of different nuclei that have a Cr concentration of $C_{\mathrm{Cr}}^{\mathrm{P,eq}}$ inside the nucleus, and a smooth interface between the matrix and the nucleus. Figure 6(a) shows the concentration profile of the classical critical nucleus for given Cr overall concentration $c_0 = 0.16$ at temperature $T = 500$ K. For comparison, the concentration profile of the non-classical critical nucleus from the CSDD method is shown in the same figure. We can see that the classical and non-classical nuclei have quite different concentration profiles. Analyzing the evolution of the classical nucleus, it is interesting to find that the nucleus first shrinks to a critical state and then grows. Figure 6(b) shows the evolution of the classical nucleus at the shrinkage stage. The concentration profile of the nucleus at the critical state is plotted in figure 6(c). The non-classical critical nucleus predicted from the CSDD method is plotted in the same figure for comparison. We can see that the

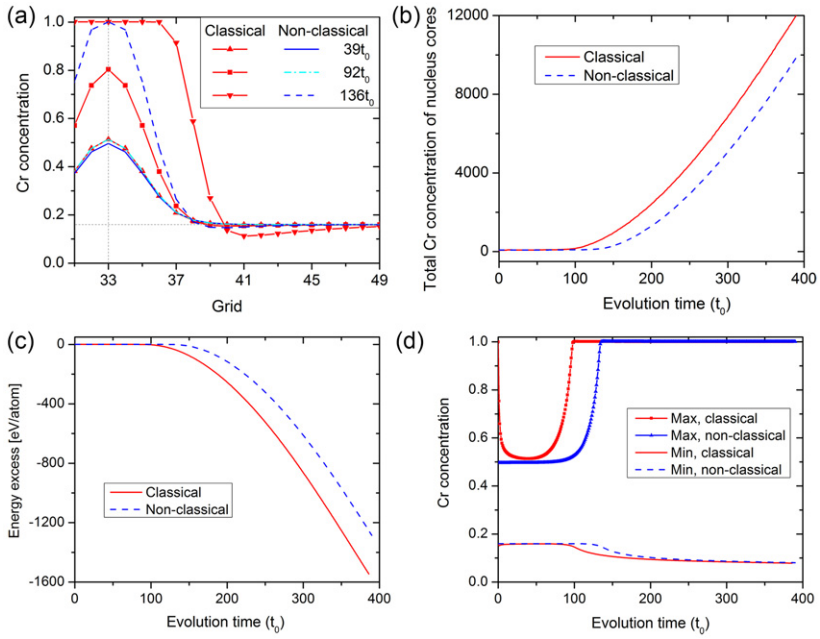

Figure 7. Comparison of the growth kinetics of the non-classical nucleus and classical nucleus. (*a*) Nucleus profile evolution with time. The dashed and solid lines represent the evolution of the non-classical nucleus. The lines with symbols represent the evolution of the classical nucleus. Only partial profiles are shown for clarity. Grid point 33 is the center of the spherical nuclei. (*b*) Total Cr concentration inside the nucleus cores. The core is defined as with $C_{\mathrm{Cr}} \geqslant 0.20$. The total Cr concentration in the simulation cell is $64 \times 64 \times 64 \times 0.16 = 41943$. (*c*) Evolution of the energy excess. (*d*) The evolution of maximum concentration inside the nucleus and minimum concentration in the matrix.

concentration profile at the critical state is almost the same as that of the non-classical nucleus. The temporal evolution at the growth stage is depicted in figure 6(*d*). The results show that the classical nucleus concentration profile first evolves to the non-classical nucleus concentration profile, which further proves the capability of the CSDD method in searching for critical nuclei.

The evolution kinetics of classical and non-classical nuclei is then compared. Figure 7(*a*) shows the comparison of Cr concentration distribution evolution. Since the maximum concentration varies with time, the radius of the nucleus could not reflect the growth kinetics. We analyze the evolution of the total Cr contents in Cr precipitates, which are plotted in figure 7(*b*). Both figures 7(*a*) and (*b*) show that the classical nucleus grows faster at the early growth stage than the non-classical nucleus. By examining the total amounts of Cr in the classical and non-classical nuclei that are shown in figure 6(*a*), we can easily find that the difference of their growth kinetics can be attributed to the facts that: (1) the classical critical nucleus requires more Cr than the non-classical nucleus; and, (2) when the classical nucleus shrinks to the critical state, the extra Cr causes a higher supersaturation around the nucleus compared to the non-classical nucleus. If we compare the similarity of the two curves in figure 7(*b*), we can find that the growth of the non-classical nucleus has a certain time delay. In classical nucleation theory, the diffusion-controlled growth of a spatial particle can be described by $R = \lambda(Dt)^{1/2}$; where, R is the radius of the particle, D is the diffusivity,

t is time, and λ is a dimensionless growth parameter which depends on the supersaturation and the particle size [16]. It is clear that the growth of a non-classical nucleus does not follow the growth kinetics of classical diffusion-controlled growth. The non-classical nucleus has a very small driving force when it starts to grow from the critical nucleus profile because the critical nucleus is a saddle point. The time to get away from the saddle point is non-ignorable compared to the time that the center point of the nucleus reaches to its equilibrium value. A profile with its equilibrium value at its center point belongs to the classical nuclei. Figures 7(c) and (d) plot the evolution of the energy excess and maximum concentrations inside the nucleus and the minimum concentration in the matrix. We can see that in the energy excess, the maximum and minimum concentration change very slowly during the time to get away from the saddle point. After getting away from the saddle point, the growth of the nucleus speeds up. The energy excess then starts to decreases sharply. The maximum concentration increases and the minimum concentration decreases. The nuclei gradually reach their thermal equilibrium concentrations, as shown in figure 7(d). The nucleus growth then follows the diffusion-controlled growth. The growth kinetics of the classical nucleus is different from that of the non-classical nucleus. The big differences are that: (1) Cr concentration inside the nucleus first reduces, then increases and (2) it takes a shorter time to get transition from decreasing to increasing of Cr concentration inside the nucleus. These results demonstrate that the non-classical nucleus at the early growth stage has a different growth kinetics from that predicted by the classical diffusion-controlled growth theory. The deviation of the nucleus concentration profiles introduced in a phase-field model could result in a profound effect on growth kinetics. Therefore, to correctly capture the kinetics of precipitation, it is critical to introduce the correct critical nuclei.

7. Conclusions

Using the thermodynamic and kinetic properties of FeCr alloys from CALPHAD calculations and atomistic simulations, the CSDD and phase-field method have been able to quantitatively predict the critical nucleus concentration profiles, nucleation energy barriers, and growth kinetics of Cr precipitates in FeCr alloys. It is found that the critical nuclei of Cr precipitates from the CSDD method are non-classical because the concentration inside the nuclei is much smaller than the thermal equilibrium concentration calculated from the equilibrium phase diagram. These results are in agreement with atomic probe observation. The simulations of critical nucleus evolution showed a number of interesting phenomena, including: (1) a critical classical nucleus first shrinks to a non-classical nucleus and then grows; (2) a non-classical nucleus has much slower growth kinetics at the earlier growth stage when compared to the diffusion-controlled growth kinetics and (3) a critical classical nucleus grows faster at the earlier growth stage than the non-classical nucleus. All of these results demonstrate that it is essential to introduce the correct critical nuclei in order to correctly capture the kinetics of precipitation.

Acknowledgments

This research was supported by the US Department of Energy's Nuclear Energy Advanced Modeling and Simulation (NEAMS) Program in Pacific Northwest National Laboratory (PNNL), which is operated by Battelle Memorial Institute for the US Department of Energy under Contract No DE-AC05-76RL01830.

References

[1] Klueh R L and Harries D R 2001 *High-chromium Ferritic and Martensitic Steels for Nuclear Applications* (West Conshohocken, PA: ASTM) MONO3
[2] Grobner P J 1973 *Metall. Trans.* **4** 251–60
[3] Mohapatra J N, Kamada Y, Kikuchi H, Kobayashi S, Echigoya J, Park D G and Cheong Y M 2011 *IEEE. Trans. Magn.* **47** 4356–9
[4] Scott P 1994 *J. Nucl. Mater.* **211** 101–22
[5] Chen L Q 2002 *Annu. Rev. Mater. Res.* **32** 113–40
[6] Novy S, Pareige P and Pareige C 2009 *J. Nucl. Mater.* **384** 96–102
[7] Bonny G, Terentyev D and Malerba L 2008 *Comput. Mater. Sci.* **42** 107–12
[8] Caro A, Caro M, Klaver P, Sadigh B, Lopasso E M and Srinivasan S G 2007 *JOM* **59** 52–7
[9] Schwen D, Martinez E and Caro A 2013 *J. Nucl. Mater.* **439** 180–4
[10] Chen L Q and Shen J 1998 *J. Comput. Phys. Commun.* **108** 147–58
[11] Sadigh B and Erhart P 2012 *Phys. Rev.* B **86** 134204
[12] Zhang L, Chen L Q and Du Q 2007 *Phys. Rev. Lett.* **98** 265703
Zhang L, Chen L Q and Du Q 2010 *Commun. Comput. Phys.* **7** 674–82
[13] Zhang L, Chen L Q and Du Q 2008 *Acta Mater* **56** 3568–76
Zhang L, Chen L Q and Du Q 2010 *J. Comput. Phys.* **229** 6574–84
[14] Zhang J and Du Q 2012 *SIAM J. Numer. Anal.* **50** 1899–921
[15] Zhang J and Du Q 2012 *J. Comput. Phys.* **231** 4745–58
[16] Rivera-Diaz-del-Castillo P E J and Bhadeshia H K D H 2001 *Mater. Sci. Technol.* **17** 25–9